LIMNOLOGY
and
OCEANOGRAPHY

ASLO

Limnol. Oceanogr. 00, 2015, 00–00

doi: 10.1002/lno.10089

Sediment transport dynamics near a river inflow in a large alpine lake

K. R. Scheu,* D. A. Fong, S. G. Monismith, O. B. Fringer
Environmental Fluid Mechanics Laboratory, Stanford University, Stanford, California

Abstract

Sediment dynamics were investigated in Lake Maggiore, Italy, with field observations from October to mid-December 2012. Three moorings were deployed in Pallanza Bay, a small embayment on the western side of the lake near the Toce River inflow, to measure temperature and currents throughout the water column and suspended sediment concentration (SSC) was estimated with acoustic instrumentation. River intrusions are shown to dominate observed SSC, although a small amount of sediment resuspension was observed at the site of the shallowest mooring during a large wind event that produced strong upwelling of the thermocline followed by downwelling. Although vertical turbulent sediment flux is typically assumed to indicate resuspension and the upward transport of sediment ($\overline{w'c'} > 0$), downward turbulent sediment flux was observed ($\overline{w'c'} < 0$) near the bed during the largest observed intrusion event. The downward turbulent sediment flux significantly contributes to net deposition rates, which are one order of magnitude larger than rates of erosion measured during the two major events observed. Horizontal transport of sediment occurs in vertically confined layers due to buoyancy-driven intrusions. Beneath the intrusions, sediment settles out of the water column at settling rates that appear to be constant with depth based on acoustic Doppler current profiler backscatter measurements. The effective settling velocities needed to produce the observed vertical transport of SSC during an inflow intrusion are one order of magnitude larger than those due to the Stokes settling velocity (w_s) alone. Particle flocculation and possible convective instabilities may play a role in generating the large observed effective settling rates.

Suspended sediment concentration (SSC) can significantly affect the ecological health and function of lakes and reservoirs. Sediment can regulate primary production by limiting light availability and also by acting as a source of nutrients (Schallenberg and Burns 2004). High sediment concentrations in a lake or reservoir can lead to poor water quality from high turbidity levels as well as decreased basin volume through sedimentation (Morris et al. 2008). The fate of suspended sediments can control the distribution of persistent organic contaminants and can also affect the availability of these pollutants to aquatic species (Schoellhamer et al. 2007). Lakes and reservoirs can act as sinks for many sediment-bound contaminants that can accumulate and deleteriously affect aquatic ecosystems (Mariani et al. 2008). Additionally, clean sediment inputs to the system can potentially lead to natural recovery of certain sediment-bound pollutants. Understanding the mechanisms governing sediment transport and the relative rates of sediment processes such as deposition, erosion, and settling can be key to understanding how a lacustrine ecosystem will be impacted.

*Correspondence: kscheu@stanford.edu

River inflows are often the dominant source of nutrients, sediments, and contaminants into a lake or reservoir; thus, the fate of these river-borne constituents depends on the hydrodynamics of the river plume as it enters the lake or reservoir (Rueda and MacIntyre 2010). A river flowing into a body of water will lead to an overflow that propagates along the surface if the river water is less dense than the ambient lake water, or, if it is more dense, the river water will plunge beneath the surface as an underflow (Alavian et al. 1992). If the plume reaches a depth of neutral buoyancy, it will intrude into the water column, forming an inflow intrusion. The depth and the vertical extent of the intrusion are dependent on the initial density of the river inflow, the ambient stratification, and the amount of mixing between water masses (Alavian et al. 1992). A laterally bounded or approximately two-dimensional (2D), buoyancy-driven intrusion of thickness h will propagate at its depth of neutral buoyancy with a speed roughly equal to $U \approx 0.2Nh$ (Manins 1976; Ford and Johnson 1983), where the average buoyancy frequency across the intrusion is given by $N=(g\Delta\rho/\rho_o h)^{1/2}$, where $\rho_0 = 1000$ kg m^{-3} is the reference density of water and $\Delta\rho$ is the density difference across the intrusion. In a large lake, rotation will influence the trajectory of the plume and

can also act to laterally confine the plume against a boundary. In this case, the width of the plume in the lateral direction is given approximately by $b \sim (QN/f^2)^{1/3}$, where Q is the volume flow rate of the intrusion and f is the Coriolis frequency (Imberger and Hamblin 1982).

A growing body of research has investigated the complex mixing and hydrodynamics of sediment-laden river inflows in the near field. However, the ultimate fate of suspended sediment from an inflow intrusion in the far field has received limited attention. The vast majority of research investigating the fate of sediments from an intrusion has focused on numerical modeling with limited observations for model validation (DeCesare et al. 2006; Umeda et al. 2006; Chung et al. 2009). This is largely due to the difficulty in measuring sediment concentration as well as the intermittent nature of inflow intrusions. Furthermore, long time records are required to investigate the timing of sediment delivery and the eventual rates of deposition from an intrusion. Observations of sediment laden intrusions have largely been conducted with transects along the length of the plume that provide a snapshot in time (Best et al. 2005; Vidal et al. 2012). A small number of studies have been conducted with moored observations (Chikita 1990; DeCesare et al. 2006). These are limited in spatial extent but allow for investigation of the time dependence of sediment delivery.

Although river inflows are often the dominant source of sediment to a lake or reservoir, sediment and its constituents can be reintroduced to the water column through sediment resuspension with subsequent redistribution in a system. Sediment erosion and resuspension are initiated due to shear stress exerted on the bed by the flow. More specifically, resuspension occurs when the bed shear stress, τ_b, exceeds the critical bed shear stress, τ_{crit}, which is assumed to be a property of the bed material and depends on factors including sediment particle size, bed consolidation, and physiochemical properties (Winterwerp and van Kesteren 2004). The bed shear stress can be estimated in field observations with measurements of the near-bed Reynolds stress (Trowbridge et al. 1999). Sediment resuspension has been neglected in prior studies of Lake Maggiore although no direct near-bed measurements have been made (Callieri 1997). The largest bottom shear stresses, and therefore, the most likely locations of sediment resuspension, have been shown to occur where the oscillating thermocline intersects the bottom of the lake (Münnich et al. 1992; Gloor et al. 1994; Lorke 2007), which is typically around 20-40 m in Lake Maggiore. Therefore, internal interface motions have the potential to resuspend sediment around the depth of the thermocline and transport it into the lake interior. We show that this mechanism is negligible when compared to sediment delivered by river inflows.

The objective of the work presented here is to investigate the dominant mechanisms governing sediment transport in a large alpine lake near a river inflow. The observations are made over a relatively long time period of two and one half months with moored instrumentation measuring velocity and temperature throughout the water column. Adjusted acoustic backscatter measurements are used as a proxy for SSC throughout the water column during the record and near-bed SSC and turbulent sediment flux measurements are obtained with a laboratory calibration (methods discussed in detail below). Near-bed rates of both sediment resuspension and deposition are derived from vertical turbulent sediment flux measurements. Additionally, the moored instrumentation provided observations of horizontal sediment transport rates arising from inflow intrusions between two sites as well as observations of the effective rate of sediment settling through the water column below an intrusion.

The content of the article focuses on measurements made during two dominant events, which we refer to as Events I and II. Event I was a wind event that generated thermocline displacement and sediment resuspension. The physics of this event are verified qualitatively with the three-dimensional (3D) hydrodynamic model. Event II was a large inflow intrusion that generated elevated SSC measurements throughout the water column. During the inflow intrusion, the near-bed vertical turbulent sediment flux contributes to net deposition due to the shape of the sediment concentration profile near the bed. We show that river intrusions are the primary source of observed SSC over the deployment and compare the rates of resuspension and deposition during the two events. Additionally, the rate of horizontal sediment transport between two sites is shown to compare well with 2D intrusion velocity scaling and the effective rate of observed sediment settling from an inflow intrusion was an order of magnitude larger than the expected Stokes particle settling.

Methods

Study site overview

A field study was conducted in Lake Maggiore, Italy with measurements concentrated in Pallanza Bay (Fig. 1). Pallanza Bay is characterized by very steep slopes on its northern and southern boundaries with a more gradual slope in the center of the bay, which plateaus at a depth of approximately 120 m and then rapidly deepens where the bay connects to Lake Maggiore. The hydrodynamics in the bay are forced by river inflows, winds, and seasonal heating and cooling. The river inflow from the Toce River (shown in Fig. 1) is driven by snowmelt in the spring and by storms in the fall and is also influenced by hydropower dams and reservoirs more than 100 km upstream. The winds are generally oriented along the main axis of the lake and are typically from the northwest or southeast in Pallanza Bay. The lake dynamics are seasonally dependent with strong temperature gradients during the summer and fall due to heating of surface waters, with mixing and cooling of the surface waters during the winter.

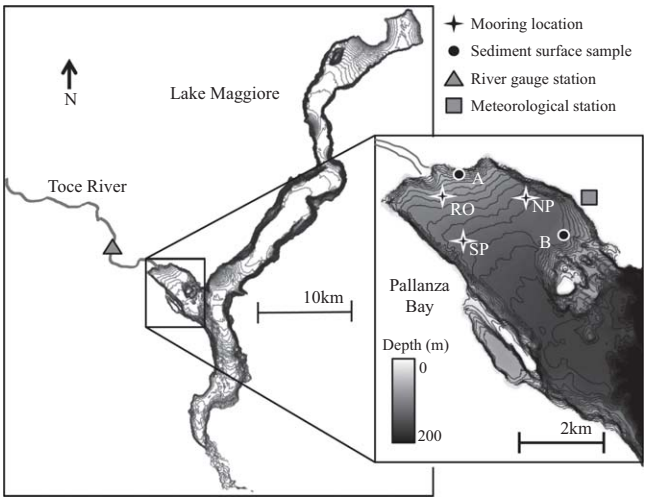

Fig. 1. Bathymetry of Lake Maggiore with bathymetric contours plotted every 10 m. Pallanza Bay is shown in the zoomed-in panel on the right. The extents of the smaller panel are 45.87° to 45.94° N latitude and 8.48° to 8.56° E longitude. Mooring sites RO (River Outlet), SP (South Pallanza), and NP (North Pallanza) are indicated by black stars. Also indicated are the locations of the sediment surface grab samples (black circles), the meteorological station (gray square), and the river stage station (gray triangle).

The average sedimentation rate in Pallanza Bay is approximately 3–10 mm annually with the highest sedimentation rates occurring near the river mouth (Marchetto et al. 2004). Over one hundred cores have been taken throughout the bay and have shown that the bed is composed of silts and clays with the exception of some small fractions of sand near the Toce River mouth at < 2 m depth (Jones 2012). A medium-sized silt with grain diameter of 0.016 mm has a Stokes settling velocity of 1.4×10^{-4} m s^{-1} and a medium-sized clay sediment particle with a diameter of 0.002 mm has a settling velocity of 2×10^{-6} m s^{-1}. Therefore, the Stokes settling velocity of a single sediment particle in Pallanza Bay away from the immediate river mouth is expected to be relatively small and on the order of $O(10^{-4}-10^{-6})$ m s^{-1}. The minimum critical shear stress required to resuspend sediment in Pallanza Bay was found to be approximately 0.1 Pa (or a Reynolds stress of 1×10^{-4} m^2 s^{-2}, assuming a water density of $\rho = 1000$ kg m^{-3}) based on Sedflume analysis of cores throughout the bay (Jones 2012).

Instrumentation

The data used in this study was collected during a field campaign from 05 October 2012 to 15 December 2012. This period was chosen to ensure that the lake was still strongly stratified from summer heating to investigate the influence of stratification as well as to capture large fall storm events and corresponding river inflow dynamics that are expected to be important for sediment transport and deposition. The field study consisted of three moorings located in Pallanza Bay at the sites indicated in Fig. 1. One site was on the shallower, northern side of the bay at approximately 100 m depth (site NP—North Pallanza); a second site was in the deeper, southern side of the bay at approximately 115 m depth (site SP—South Pallanza); and the last site was at the western end of the bay near the river mouth at approximately 60 m depth (site RO—River Outlet). The site locations were constrained by fishing regulations that prevented placement of the moorings further into the interior of the bay. However, the chosen locations allowed for measurement of along- and cross-bay variability.

Each mooring consisted of a frame that supported an upward-facing Teledyne RDI acoustic Doppler current profiler (ADCP) and two downward-facing Nortek acoustic Doppler velocimeters (ADVs). A thermistor chain with five meters vertical resolution was also deployed at each site. A 600 kHz ADCP with 10 s temporal resolution and four meters vertical resolution was deployed at site RO (the shallowest mooring site). A 300 kHz ADCP with 15 s temporal resolution and eight meters vertical resolution was deployed at both sites NP and SP. The 6 MHz ADVs sampled in six-minute bursts at 1 Hz (the sampling rate was shown to be sufficient to resolve the inertial dissipation range down to the noise level of the ADV) every hour and measured at approximately 0.65 m and 0.35 m above the bed at each mooring location. Meteorological data (wind speed and direction, air temperature, rainfall, humidity, pressure, and radiation) were measured on the northern side of the bay (indicated by the gray rectangle in Fig. 1) and river inflow was measured slightly upstream of the river mouth at Candoglia river station (indicated by the gray triangle in Fig. 1).

Suspended sediment transport

Owing to the dominance of fine-grained sediment (silts and clays) flowing into Pallanza Bay, we assume that the sediment transport is dominated by suspended sediment load and bed-load transport is negligible. The governing equation for SSC transport is obtained by decomposing the concentration (c) into its time-averaged ($\bar{c}$) and fluctuating parts (c'), $c = \bar{c} + c'$. Although the sediment dynamics and hydrodynamics in Pallanza Bay are complex and 3D, we will simplify the equation to focus on the SSC along a 2D transect that follows the trajectory of a typical sediment particle as it exits the river and flows into the bay. In the 2D formulation below, the cross flow advection and dispersion terms have been neglected. This is generally a good approximation for a river inflow, particularly if it is laterally confined (either by physical boundaries or rotational effects), although lateral spreading may be important in some phases of the development of the river plume. If x is defined as the distance from the river mouth and z is the distance from the free surface of the bay (positive upward), the governing equation for SSC along this transect can be approximated with

$$\frac{\partial \bar{c}}{\partial t}+\frac{\partial}{\partial x}(\bar{u}\,\bar{c})=\frac{\partial}{\partial x}\left(K\frac{\partial \bar{c}}{\partial x}\right)-\frac{\partial}{\partial z}(\bar{w}\,\bar{c})+\frac{\partial}{\partial z}(w_s\bar{c})-\frac{\partial}{\partial z}(\overline{w'c'}) \quad (1)$$

where $\bar{u}$ is the time-averaged horizontal velocity (positive into the bay), $\bar{w}$ is the time-averaged vertical velocity (positive upward), $\overline{w'c'}$ is the vertical turbulent sediment flux, w_s is the Stokes settling velocity ($w_s > 0$), and K is the longitudinal dispersion coefficient arising from along-axis plume spreading (Bedford et al. 1987). The SSC as a function of time can therefore be modified by along-axis spreading, gradients in the horizontal advective flux per unit area of sediment, $\bar{u}\,\bar{c}$, and gradients in the vertical flux per unit area of sediment, which are comprised of vertical advective flux, $\bar{w}\,\bar{c}$, gravitational settling flux, $w_s\bar{c}$, and vertical turbulent sediment flux, $\overline{w'c'}$.

The vertical turbulent sediment flux ($\overline{w'c'}$) measured near the bed has been used widely to approximate sediment erosion and can be measured directly with the ADVs used in this study (Brennan et al. 2002; Voulgaris and Meyers 2004; Yuan et al. 2008). When $\overline{w'c'} > 0$, positive concentration fluctuations of sediment correspond to upward velocities ($w' > 0$, $c' > 0$) or negative concentration fluctuations correspond with downward velocities ($w' < 0$, $c' < 0$) generating a net upward flux of sediment, indicating sediment resuspension when measured near the bed. The occurrence of sediment resuspension can be further verified by comparing the critical bed Reynolds stress required for resuspension of Pallanza Bay sediments with measured values of the near-bed Reynolds stress ($\overline{u'w'}$). In the work presented here, the Reynolds stress and turbulent sediment fluxes were measured at 0.35 m and 0.65 m above the bed. We found that the measurements of the Reynolds stress at both locations were approximately equal to each other, suggesting a region of near-constant stress near the bed. Therefore, we assume that the stress at the bed is well approximated by stress measured just above the bed. Similarly for the turbulent sediment fluxes, the values measured just above the bed are roughly constant at the two locations, and therefore, the measured values are used to approximate the fluxes into or out of the sediment bed (deposition or erosion). This method of estimating bed erosion using near-bed measurements has been widely used in literature (Brennan et al. 2002; Voulgaris and Meyers 2004; Yuan et al. 2008). Time-averaged values (indicated by the overbar) are averaged over the six-minute burst interval of the ADV measurements and the fluctuating components are deviations from the burst-averaged mean.

The vertical turbulent sediment flux, $\overline{w'c'}$, is typically assumed to transport sediment upward through the water column (van Rijn 1984) and numerous studies have assumed a balance between upward turbulent sediment flux, $\overline{w'c'}$, and downward gravitational sediment settling, $w_s\bar{c}$ (Kawanisi and Yokosi 1997; Fugate and Friedrichs 2002; Brand et al. 2010). This balance gives rise to the well-known Rouse profile in which the peak in the SSC occurs at the bed and rapidly decays away from the bed as a function of the shear velocity and settling velocity. Assuming a balance between downward settling and upward turbulent flux is useful because the settling velocity can be estimated with quantities that can be measured, i.e., $w_s = \overline{w'c'}/\bar{c}$. However, assuming such a balance would produce meaningless settling velocities in the case of sediment delivery from a river inflow intrusion. River inflow intrusions result in an imbalance between the vertical turbulent flux and downward settling, and thereby produce sediment concentration profiles that deviate from the Rouse profile. For instance, the presence of a source of sediment from an inflow intrusion yields a large horizontal flux of sediment that produces higher SSC at the intrusion depth than near the sediment bed. The near-bed concentration profile therefore has the opposite sense ($\partial\bar{c}/\partial z > 0$) during an intrusion event. The presence of turbulence will act to mix out the gradient, suggesting that downward turbulent sediment flux ($\overline{w'c'} < 0$) may be observed. In our study, the downward turbulent sediment flux significantly contributes to the total downward flux of sediment, such that the net deposition near the bed is given by $D = w_s\bar{c} + \overline{w'c'}$ during large inflow intrusion events.

Although horizontal advection and unsteadiness will typically incur an imbalance between the settling flux and vertical turbulent flux of sediment during a river inflow event, when the river inflow event ceases, horizontal advection ($\bar{u} = 0$) and lateral spreading ($K = 0$) become negligible. Furthermore, vertical advection can be assumed to be very small ($\bar{w} \ll w_s$), although it may be significant in portions of the water column, particularly at the river mouth, or in the presence of steep bottom slopes. Therefore, after the river intrusion event, the ensuing balance can be approximated by

$$\frac{\partial \bar{c}}{\partial t}=\frac{\partial}{\partial z}(w_s\bar{c})-\frac{\partial}{\partial z}(\overline{w'c'}) \quad (2)$$

This equation implies that, after a river inflow intrusion event, the SSC in the water column will respond predominantly to both vertical turbulent flux, which in itself decreases in time as the turbulence from the intrusion decays, and vertical gravitational settling.

Suspended sediment concentration from acoustic instruments

We approximate SSC using the backscatter intensity from the acoustic instruments used in the field experiment (ADVs and ADCPs). The instruments operate by emitting acoustic pulses that are scattered back toward receivers by particulates in the water column, and the intensity of the backscattered signal is proportional to the number of sediment particulates in the water column. The backscatter intensity measured by an ADV is a function of the product ka, where k is the acoustic wave number of the instrument and a is the particle radius. When $ka < 1$, corresponding to $a < 79\,\mu m$ for a 6 MHz Nortek ADV (Voulgaris and Meyers 2004) and SSC < 1

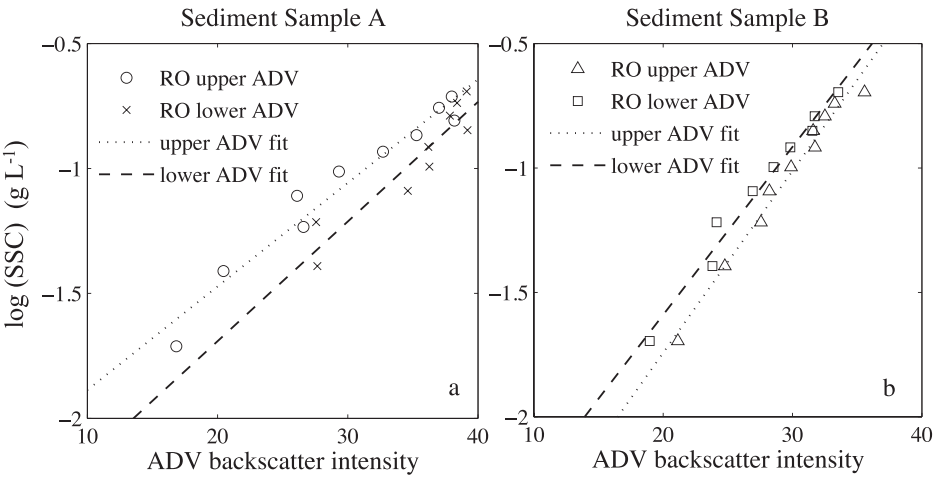

Fig. 2. Calibration curves for the 6 MHz Nortek ADVs used at site RO with (a) sediment sample A and (b) sediment sample B.

g L^{-1}, the acoustic backscatter signal, ABS, is related to SSC with

$$\log(\mathrm{SSC}) = c_1 \mathrm{ABS} + c_2 \quad (3)$$

where c_1 and c_2 are empirically determined constants (Salehi and Strom 2011). These constants are a function of properties of the sediment particles in suspension as well as the particular instrument used and operational settings. Therefore, the coefficients are valid for a particular sediment sample and for specific instrument settings. It should be noted that the backscatter intensity is also dependent on the particle size distribution. Nevertheless, the validity and theory of using an acoustic signal to calculate SSC has been well documented in the literature (Thorne and Hanes 2002; Ha et al. 2009; Salehi and Strom 2011) and has been widely used to calculate SSC from observations (Kawanisi and Yokosi 1997; Voulgaris and Meyers 2004; Brand et al. 2010). ADV backscatter intensity also gives a good approximation for cohesive sediments when the concentrations are relatively small, < 1 g L^{-1} (Maa and Kwon 2007; Ha et al. 2009; Salehi and Strom 2011), a condition easily met during our study.

We calibrated ADV backscatter intensity data with SSC in the laboratory to empirically determine the coefficients c_1 and c_2 in Eq. 3. The ideal method for calibration would be with in situ water samples of SSC throughout the record. However, this was not done because the moorings were prohibitively deep, but instead we used a laboratory calibration based on two sediment samples taken from Pallanza Bay. The sediment samples were acquired with a clamshell sediment sampler and are from the upper 10 cm and 20 cm of the sediment surface for samples A and B, respectively. Sample A was taken near the river mouth close to site RO and sample B was taken from the deeper, northern section of Pallanza Bay near site NP (*see* Fig. 1 for locations), and the samples were well mixed before the laboratory calibration. The calibration curves for the two ADVs from site RO with the two sediment samples are shown in Fig. 2, which shows that the slope of the curves, c_1, is largely dependent on the sediment sample. This may be due to grain size distributions, particle densities or particle compositions that differ between the two sediment samples. However, the offset, c_2, is dependent on the noise floor and is a unique parameter for each particular ADV. The observed variability in slope and offset with specific sediment samples and ADVs are consistent with previous calibrations in the literature (Brand et al. 2010). In the following analysis, the coefficients used to determine SSC at site RO were taken from the calibration with sediment sample A. The coefficients used for site SP were taken from calibration with sediment sample B. These selections were based on the proximity of the sediment samples to the sites as well as the relative distance from the river mouth (coarser grains are expected closer to the river mouth). Sediment data from site NP will not be presented because the backscatter signal throughout the record was extremely small indicating that significant sediment concentrations were not observed in the water column at site NP.

Before the ADV backscatter data was converted to SSC, the backscatter signal was processed to remove outliers. The outliers were identified as data points in which the backscatter from one of the beams differed by more than 3% from the three-beam mean and where the mean was greater than five standard deviations from the six-minute burst mean (Brennan et al. 2002). The velocity data was processed using an iterative adaptive Gaussian filter for each burst period where values beyond three standard deviations from the mean were removed, following manufacturer suggestions. Using the coefficients determined in the laboratory calibrations, the ADV measurements provided both burst averaged

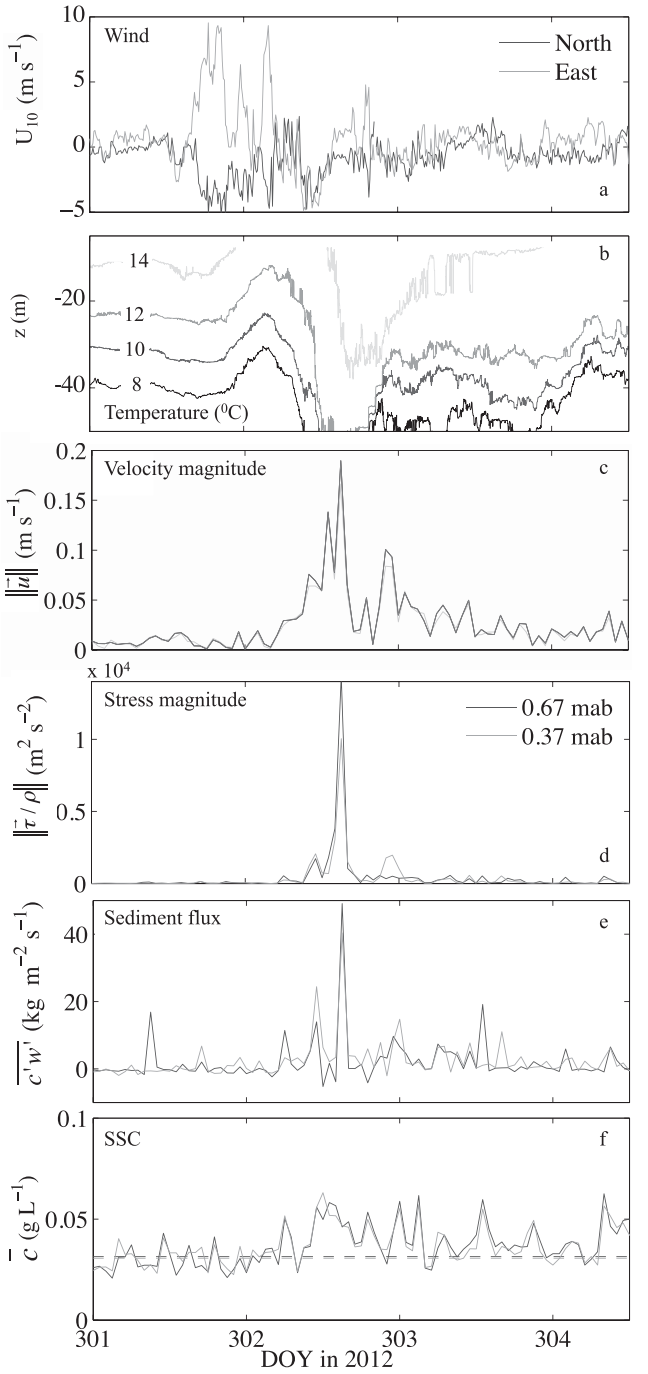

Fig. 3. Observations near the bed at site RO during event I. (a) Wind forcing during the time period; (b) lines of constant temperature (isotherms) as a function of water depth and time with the shade of gray indicating the temperature in °C; (c) the magnitude of the horizontal velocity where $\|\vec{u}\|=(u^2+v^2)^{1/2}$; (d) magnitude of the shear stress where $\|\vec{\tau}/\rho\|=(\overline{u'w'}^2+\overline{v'w'}^2)^{1/2}$; (e) sediment flux (positive indicates sediment moving upward into the water column); and (f) SSC with the dashed line indicating the average SSC over the full record. The light gray line in (c), (d), (e), and (f) indicates data from the lower ADV and the dark gray line indicates data from the upper ADV.

(time-averaged over the six-minute measurement bursts) sediment concentrations, $\bar{c}$, and turbulent sediment fluxes, $\overline{w'c'}$, near the bed.

The ADCP backscatter intensity was also processed to infer SSC profiles throughout the water column in terms of adjusted ABS. The raw ADCP acoustic backscatter intensity attenuates as a function of distance from the transducer head due to water absorption and beam spreading (Deines 1999; Gartner 2004). The raw echo intensity recorded by the ADCP, EI, was converted to an adjusted ABS using

$$\mathrm{ABS}=SF(\mathrm{EI}-E_r)+\mathrm{BS}+\mathrm{WA} \tag{4}$$

where E_r is the reference level of the echo intensity and was taken as the minimum recorded value of each beam, SF is a beam specific scale factor (acquired from the manufacturer) that converts the echo intensity in counts into dB, BS is a beam spreading term, and WA is a water absorption term (Gartner 2004). The acoustic absorption coefficient of water is dependent on water temperature and was calculated as a function of depth using interpolated values of the temperature measured by the thermistor chain. The ABS can then be converted into SSC using the same equation used for the ADVs (Eq. 3 above), where the coefficients are chosen to provide the best fit to directly measured values of SSC. There were no direct measurements of SSC at the location of the ADCP measurements and a laboratory calibration was not feasible. However, the shape of the suspended sediment curves and the timing of the peaks in concentration, rather than the exact measured values of SSC, are the primary focus of our discussion. Therefore, in what follows, the ABS data measured by the ADCPs is used as a proxy for SSC in the water column away from the bed.

Numerical modeling

A hydrodynamic model was used to help qualitatively understand the physics of the observed wind Event I. The model consisted of the 3D, unstructured-grid, hydrodynamic SUNTANS model (Fringer et al. 2006) along with a suspended sediment transport module and the Mellor-Yamada 2.5 turbulence closure scheme (Mellor and Yamada 1982). A simulation of the entire Lake Maggiore consisted of an unstructured grid with 50 m horizontal resolution in Pallanza Bay, which becomes coarser and as large as 250 m in the main lake. The grid had 40 vertical z-levels over the depth with vertical stretching such that Δz = 1.5 m near the surface and Δz = 30 m at the bottom of the lake at 370 m. The model was hydrostatic and scalar advection of temperature and SSC was computed with a monotonic flux-limiting scheme (Chua and Fringer 2011). The time step size was two seconds (dictated by the stability of explicitly computed internal gravity waves) and the background vertical and horizontal diffusivities were set to 10^{-3} m^2 s^{-1} and 10^{-2} m^2 s^{-1}, respectively. A constant Coriolis parameter with $f=10^{-4}$ rad s^{-1} was used. The initial temperature structure in the lake

was based on measured temperature values taken just before the simulated event occurred. Wind forcing alone was used to simulate Event I and no river inflow or sediment modeling was included. In this article, we report only on the results of the model at the observed mooring sites. Analysis of the 3D results and SSC transport is left to a future study that focuses on seasonal variability of the river plume.

Results

The hydrodynamics observed in the field record in Pallanza Bay were characterized by intermittent strong events flanked by relatively quiet periods. Over the field record, two major events were observed and are discussed in depth below. The first event (Event I) was a large wind event at the end of October that generated a small amount of sediment resuspension at Site RO. A large inflow event (Event II) was observed at the end of November that formed an intrusion and corresponded to the largest measured values of SSC throughout the record.

Elevated shear stress and sediment resuspension during Event I

Over the measurement period, upward sediment flux ($\overline{w'c'} > 0$) indicating sediment resuspension occurred only during Event I and at site RO, the shallowest site near the river. The peak in upward sediment flux corresponded to a large peak in the near-bed Reynolds stress that exceeded the critical stress of 1×10^{-4} m^2 s^{-2}. Although elevated Reynolds stresses were observed at sites SP and NP that peaked at 3×10^{-5} m^2 s^{-2} and 1×10^{-5} m^2 s^{-2}, respectively, no sediment resuspension was observed at these sites because the critical Reynolds stress was not exceeded.

During Event I, a large wind stress (Fig. 3a) was observed that peaked on 27 October and corresponded to a gradual elevation of the isotherms at site RO (Fig. 3b). The relaxation of the wind coincides with a large depression of the isotherms as well as a peak in the magnitude of the horizontal velocity (Fig. 3c), the magnitude of the near-bed shear stress (Fig. 3d), and upward turbulent sediment flux (Fig. 3e), indicating sediment resuspension. However, the elevated Reynolds stress and upward sediment flux correspond to a very small local increase in SSC (Fig. 3f). At sites SP and NP, 10-20 m amplitude fluctuations in the isotherms were also observed (not shown), although sediment resuspension did not occur at these sites because they are significantly deeper and therefore the currents induced by thermocline motion are negligible at this depth.

The observations suggest that the large temperature fluctuations and the large bottom shear stress in Pallanza Bay during Event I are due to wind-driven upwelling followed by relaxation and wind reversal. The strong northwesterly wind forces the surface water in the direction of the wind, generating upwelling at the northwestern end of the bay. The relaxation and slight reversal of the wind gives rise to downwelling at the northwestern end of the bay due to the inertia of the downwelling water as well as the reversed forcing. The peak in Reynolds stress shown in Fig. 3d corresponds to the relaxation and downwelling of the thermocline as it travels past the site RO mooring during the peak in observed horizontal bottom currents.

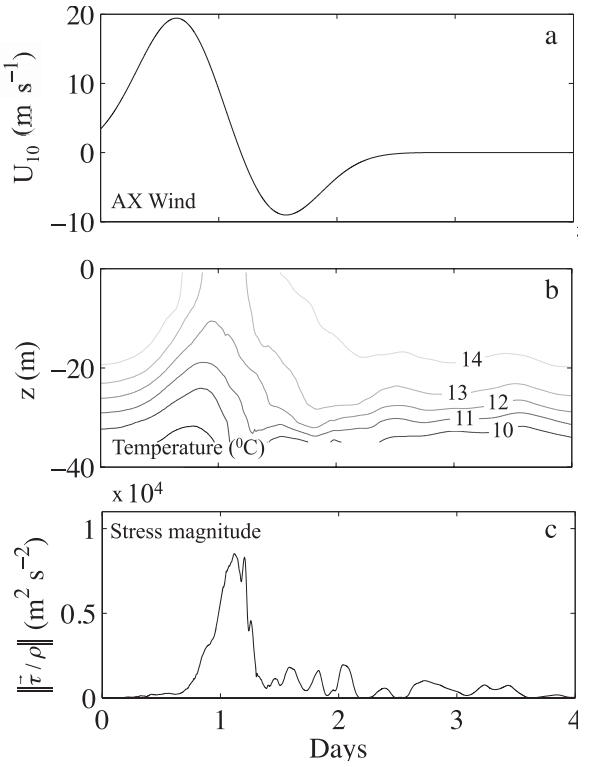

Fig. 4. Modeling results of event I. (a) Wind speed along the main axis of Pallanza Bay with positive indicating a wind toward 110°N; (b) isotherms as a function of depth and time at the approximate location of site RO (similar output to measured results shown in Fig. 3b); and (c) modeled magnitude of the bed shear stress at site RO.

Numerical modeling of Event I

Although we have described the case of upwelling in a simplified system, the actual dynamics are complex and may be influenced by factors such as the shape of the lake, the earth's rotation, and real stratification. Therefore, to verify the physics of the upwelling event, the SUNTANS model as described above was used to simulate Event I. An idealized version of the observed wind speed was used to force the model. The idealized wind peaked at 20 m s^{-1} toward the east-southeast and persisted for approximately 12 h followed by a 10 m s^{-1} peak in wind speed directed toward the west-northwest (Fig. 4a). Wind speeds used to force the model were stronger than observed wind speeds because winds are expected to be stronger over the body of the lake than at the base of the mountains where the meteorological station was positioned (Shimizu et al. 2007). The simulated isotherms

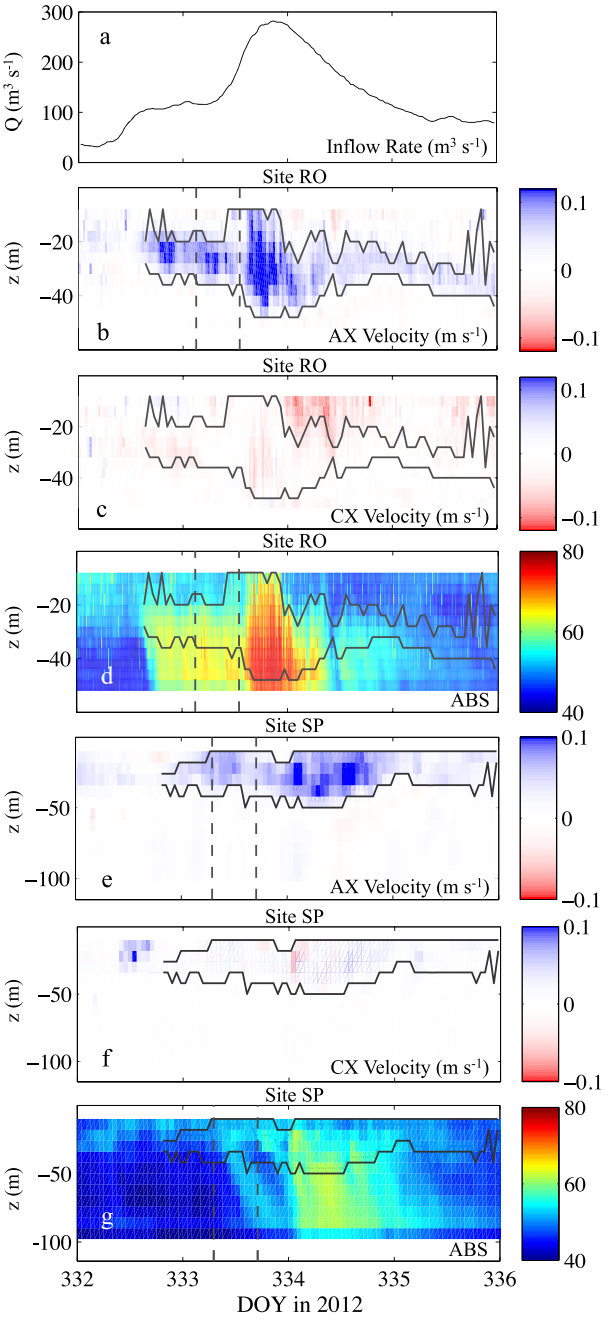

Fig. 5. Observations of velocity and ABS at sites RO and SP during event II. The velocity has been rotated by an angle θ from Northing and Easting components into principle axis components in which the along-axis component indicates the primary axis. The panels show (a) measured Toce River inflow, (b) along- and (c) cross-axis velocity at site RO rotated clockwise by $\theta = 59°$, (e) along- (f) and cross-axis velocity at site SP rotated clockwise by $\theta = 40°$, and ABS as a proxy for sediment concentration at sites RO (d) and SP (g). The dark gray lines indicate the approximate vertical extent of the intrusions where the magnitude of the AX current is 0.015 m s^{-1}.

from the event are shown in Fig. 4b at the approximate location of site RO. The model response of the isotherms is qualitatively similar to the measured response shown in Fig. 3b. Upwelling is first observed and then, due to inertia and the reversed wind forcing, downwelling occurs such that the isotherms propagate past the site RO mooring. The peak in the modeled bottom stress (Fig. 4c) occurs as the isotherms move past the mooring, similar to the observed Reynolds stress (Fig. 3c).

The measurements and model results suggest that wind forcing can generate significant displacement of the thermocline. Yet, more importantly, it is the subsequent downwelling and the propagation of the thermocline past the mooring during the wind relaxation and reversal that generates elevated bottom currents and associated large shear stresses. This is consistent with previous investigations that have shown that the largest bottom shear stresses occur where the oscillating thermocline intersects the lake bottom (Münnich et al. 1992; Gloor et al. 1994; Lorke 2007). The oscillation of the thermocline generates larger velocities and bottom currents near the depth of the thermocline. At site SP and NP, there is a slight increase in Reynolds stress due to the larger currents generated by downwelling of the thermocline. However, these sites do not experience an upward sediment flux or sediment resuspension because they are much deeper than the thermocline depth (and site RO) and the near-bed currents are not strong enough to resuspend sediment.

River inflow intrusion (event II)

Three inflow intrusions were observed over the deployment period during which the maximum observed velocities occurred in the middle of the water column at sites RO and SP, which is in contrast to wind-driven currents where velocity maxima occur at the surface. These river inflow intrusion events also coincided with large peaks in SSC throughout the water column. Data from both the ADCP and ADVs at site NP are not shown because velocity and SSC are small (in the noise) during the time period, suggesting that the river intrusion does not reach this mooring. Therefore, the following will focus on data from sites RO and SP.

Event II occurred between 27 November 2012 and 01 December 2012 and was the largest of the three river inflow events with the flow rate peaking at approximately 300 m^3 s^{-1} (Fig. 5a). The observed velocities at both sites RO and SP were rotated using a principle component analysis in which the angle of rotation, θ, was computed clockwise relative to East for the four-day event. The principle axis of the flow at sites RO and SP is in the direction of river inflow and is roughly aligned with the main axis of the bay. Positive currents are defined as directed to the southeast. The along-axis velocity at site RO (Fig. 5b) exhibits a strong peak in the middle of the water column around 30 m depth, indicating an inflow intrusion. There is some cross-axis flow at site RO

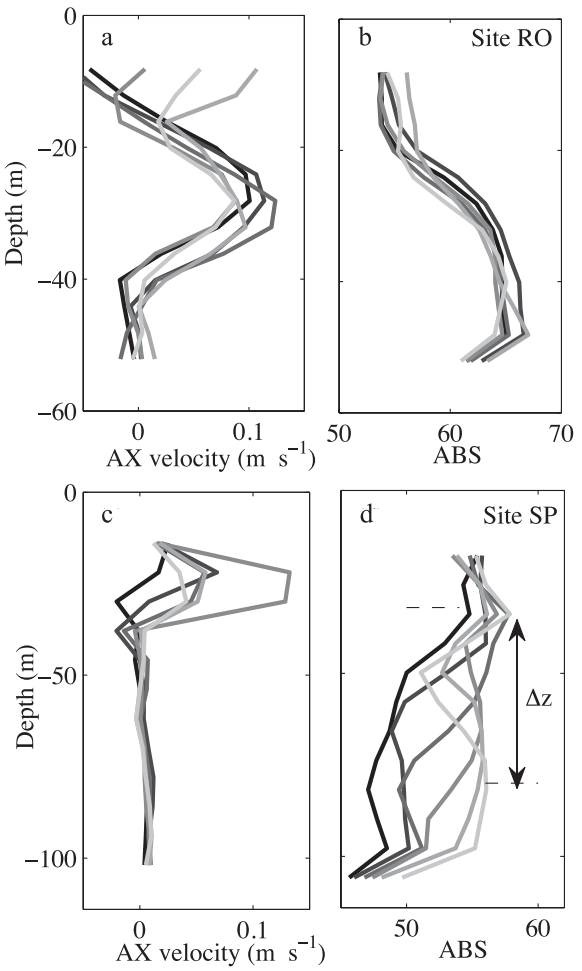

Fig. 6. Profiles of (a) along-axis velocity and (b) ABS from the ADCP at site RO as a function of depth every two hours starting on 28 November 2012 at 03:00 (black) and ending at 13:00 (lightest gray) with the lighter colors indicating later times. Similarly, profiles of (c) along-axis velocity and (d) ABS at site SP are shown starting on 28 November 2012 at 07:00 (black) and ending at 17:00 (lightest gray). The time periods containing the profiles are indicated by the vertical black dashed lines in Fig. 5b,d for site RO and Fig. 5e,g for site SP.

(Fig. 5c) at the surface, that is, likely due to wind forcing, although this has a weak impact on the intruding sediment dynamics. The along-axis velocity at site SP (Fig. 5e) also has a strong peak in velocity around 30 m depth with little cross-axis velocity (Fig. 5f). Large peaks in SSC (using ABS as a proxy) are observed at both sites RO and SP (Fig. 5d,g, respectively) although they occur slightly lower in the water column than the peaks in velocity. These measurements indicate that sediment from the river plume first passes by site RO before continuing on to site SP. The SSC decreases along this path owing to detrainment and vertical settling of sediment from the intrusion and possibly due to lateral dispersion of the plume. The dark gray lines in Fig. 5 indicate the approximate vertical extent of the inflow intrusion and are defined as the ADCP bin depth at which the along-axis velocity measurements are equal to 0.015 m s^{-1} at both sites RO (Fig. 5b,d) and SP (Fig. 5e,g).

Vertical profiles of velocity and ABS (a proxy for SSC) at specific times can inform the temporal variability of the vertical structure during an inflow intrusion. The profiles of the along-axis velocity (Fig. 6a) and ABS (Fig. 6b) at site RO are shown every two hours (later profiles are shaded progressively lighter) during the time period indicated by the dashed lines in Fig. 5b,d. Similarly, profiles of along-axis velocity and ABS at site SP (Fig. 6c,d, respectively) every two hours are from the time period indicated by the vertical dashed lines in Fig. 5e,g. At both sites, the currents induced by the intrusion remain relatively constant in time between 15 m and 50 m depth. There is some variability in the velocity at site RO at later times due to an increase in the inflow, which eventually causes the vertical scale of the intrusion to widen and results in some unsteadiness. The shape of the SSC profiles at site RO are also roughly constant over the time period, although the maxima in the SSC profiles occur deeper in the water column than those for the velocity. The SSC at site SP also exhibits persistent elevated values of SSC below the depth of the intrusion, although there is a secondary peak in the SSC that propagates downward over the 10 h time period. Assuming that the behavior of this peak corresponds only to the settling of sediment, then the settling velocity needed for the secondary peak at site SP to descend a depth of $\Delta z = 50$ m over the 10 h time period is 1.4×10^{-3} m s^{-1}. The rate of sediment settling below the inflow intrusion at site SP will be discussed further in the next section. Additionally, the peak in SSC occurs above the sediment bed throughout all of the observed intrusions at both sites RO and SP, indicating that horizontal transport rather than local resuspension is the dominant source of sediment at these sites.

The near-bed ADV measurements at site RO respond to the river inflow event via an increase in the along-axis velocity and SSC (Fig. 7b,c, respectively) and a negative (downward) maximum in turbulent sediment flux (Fig. 7d). The along-axis direction of the horizontal velocity was computed using the same angle of rotation, θ, determined from the ADCP measurements in Fig. 5. The measured SSC is slightly larger at the upper ADV location during the time periods of elevated SSC (Fig. 7c), which is consistent with elevated values of SSC higher in the water column due to the intrusion, as discussed above with reference to Figs. 5, 6. The response at site SP is similar to that at site RO, although the maxima in velocity, SSC and turbulent sediment flux (Fig. 7e,f,g, respectively) are delayed and smaller in magnitude. The near-bed measurement location at site SP is significantly deeper than the intrusion depth and the observed along-axis velocity is actually slightly negative. We believe the reversed current near the bed was likely generated to balance the positive mass flux generated at the depth of the intrusion,

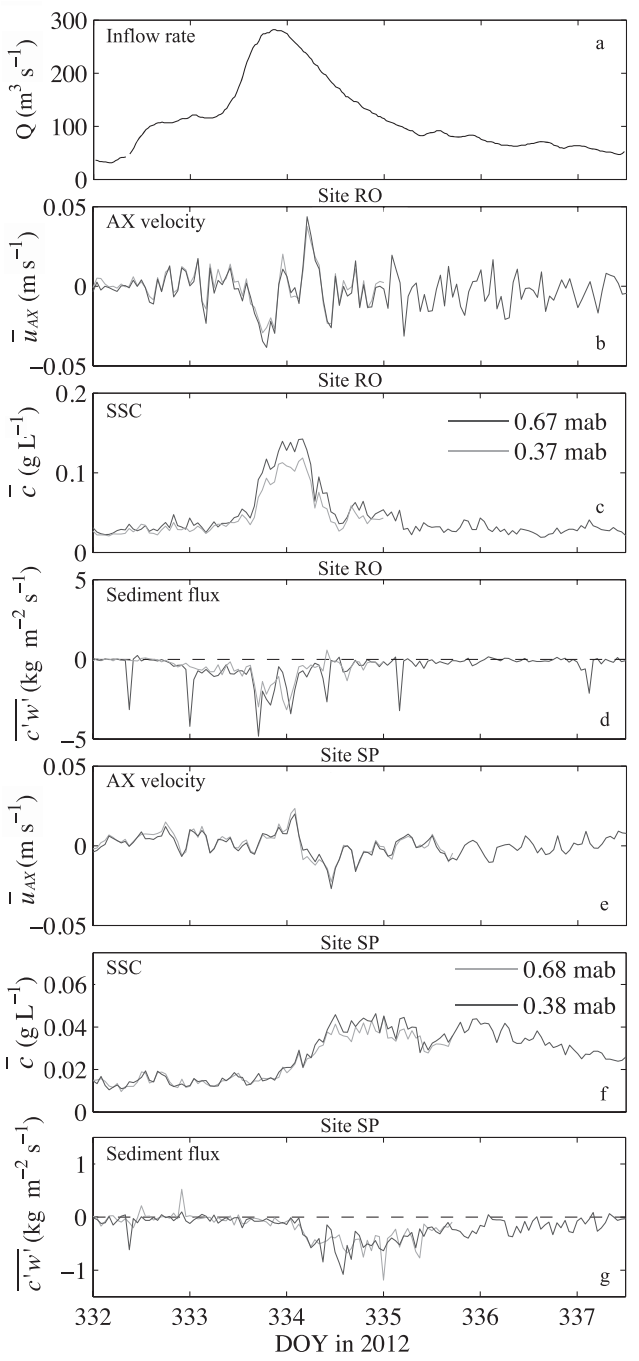

Fig. 7. River inflow and sediment transport and settling during event II. (a) Toce River flow rate; (b) along-axis velocity at site RO; (c) SSC at site RO; (d) sediment flux with the dashed line at zero at site RO; (e) along-axis velocity at site SP; (f) SSC at site SP; (g) sediment flux with the dashed line at zero at site SP. The velocity has been rotated clockwise by an angle θ from Northing and Easting components (determined from the ADCP measurements) such that $\theta = 59°$ and $\theta = 40°$ for site RO and SP, respectively. The light gray line indicates the upper ADV and the dark gray line is the lower ADV at each site.

although we leave a discussion of the details of the currents to a future manuscript in which we focus on 3D modeling of the dynamics in the unsteady river plume. During the event, the Reynolds stress peaks at approximately 2.5×10^{-5} m^2 s^{-2} and 2×10^{-6} m^2 s^{-2} at sites RO and SP, respectively, which is much less than the critical Reynolds stress of 1×10^{-4} m^2 s^{-2}. The downward turbulent sediment flux arises from the positive SSC gradient ($\partial\bar{c}/\partial z > 0$) in the lower portion of the water column during the intrusion. Turbulence near the bed will act to vertically mix the SSC gradient, generating a net downward turbulent sediment flux. Therefore, the negative peaks in turbulent sediment flux observed at both sites are due to the nature of the inflow intrusion that provides a source of sediment above the bed.

Discussion

Inflow as a primary source of SSC

The periods of elevated SSC throughout the water column coincided with large river inflow events (Event II, in particular) indicating that inflows serve as the primary source of SSC in the system. A time lagged correlation analysis was used to compare the observed Toce River inflow rate to the depth-averaged ABS data from the ADCP over the entire deployment record. The peak value of the lagged correlation coefficient, r, was 0.79 and 0.68, corresponding to a lag time (t_s) of one and nine hours, at site RO and SP, respectively. In the analysis, $r > 0.54$ corresponds to a two-sided level of significance of $p = 0.01$ with df = 20 (degrees of freedom). This strong correlation at both sites indicates that the river inflow controls the temporal variability of the observed SSC throughout the water column. In contrast, the correlations from a similar analysis between observed wind speed and SSC were not statistically significant. Additionally, during the entire deployment record, the observed Reynolds stress only exceeded the critical Reynolds stress during Event I, further indicating that the Toce River inflow is the primary source of SSC to the system rather than wind-driven resuspension. Similarly, the observed SSC at site NP and the inflow are not statistically correlated, consistent with our previous assertion that the river plume does not reach the northern site. This is due to rotational effects, which drive the plume toward and along the southern boundary of the bay.

Near-bed sediment resuspension and settling rates

The turbulent sediment flux measurements near the bed were used to determine sediment deposition and erosion rates during Events I and II. During the river inflow event (Event II), the total sediment flux is due to both Stokes particle settling, $w_s\bar{c}$, and downward turbulent sediment flux, $\overline{w'c'}$, arising from the positive near-bed vertical SSC gradient. Here the particle settling speed is estimated from the Stokes settling velocity of a medium-sized silt particle. In the case of enhanced settling due to other mechanisms (described

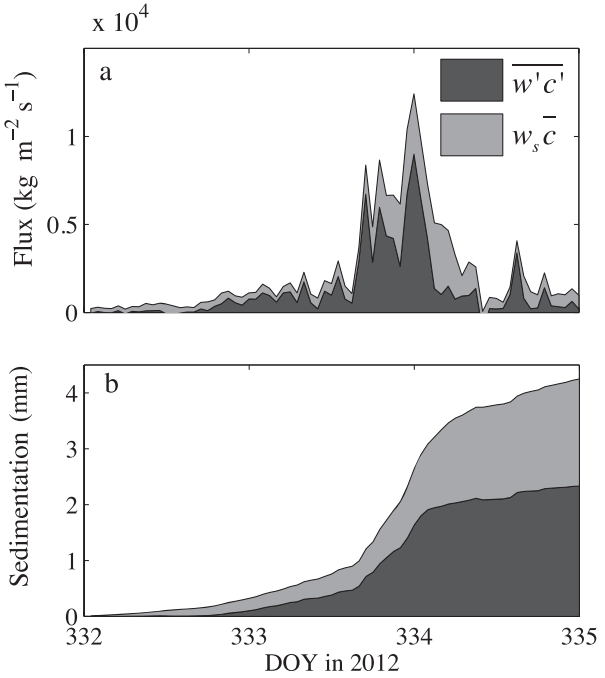

Fig. 8. Vertical sediment flux (a) and sedimentation (b) during river inflow Event II at site RO measured by the lower ADV (upper ADV yields similar results) due to both gravitational sediment settling (light gray) and downward turbulent sediment flux (dark gray).

later), the total rate of deposition will be enhanced. The total downward sediment flux measured by the lower ADV at site RO during Event II is shown in Fig. 8a. Integration of the sediment flux in Fig. 8a in time yields a cumulative sediment flux over the course of the three-day event. The cumulative turbulent sediment flux at site RO is approximately 32 kg m^{-2} and the total sediment flux, including the gravitational sediment flux term, is approximately 60 kg m^{-2} over the course of the inflow event.

The total sedimentation was estimated by dividing the cumulative flux by the wet density to yield an approximate thickness of the deposit (Fig. 8b), where the measured wet density of sediment was 1400 g L^{-1} (D. Lin, unpubl. data). This calculation yields an approximate total deposition of 4.2 mm during the three-day river inflow event, with turbulent sediment flux accounting for approximately 55% of the total settling during the event. Pallanza Bay typically receives approximately 10 mm yr^{-1} of sediment near the river mouth (Marchetto et al. 2004). This suggests that the majority of the deposition in Pallanza Bay is likely achieved with a few large river inflow events over the year as opposed to continuous, gradual deposition. This is consistent with observed SSC, which was very small during the quiet periods between inflow events at all moorings sites. Additionally, these integrated rates of deposition during the observed inflows are consistent with net deposition measurements from simultaneously deployed sediment traps in Pallanza Bay (D. Lin, unpubl. data).

The upward turbulent sediment flux observed during Event I can also be integrated to estimate the cumulative erosion of sediment. The estimated erosion during the wind event is approximately 1 kg m^{-2} over the three-day event. Dividing by the wet density, the thickness of the sediment layer eroded (using the same method) at site RO during Event I is approximately 0.7 mm. Therefore, although the instantaneous sediment fluxes are comparable in magnitude during the two events, the cumulative downward flux (or deposition) during the inflow event is one order of magnitude larger than the cumulative upward flux (or erosion) observed during the wind event. It should be noted that the acoustic backscatter is sensitive to particle size and that we might expect smaller particles to differentially be resuspended because they require a smaller shear stress for resuspension (Van Prooijen and Winterwerp 2010). Therefore the actual sediment concentration estimates during the wind event may actually be larger than those reported if there are smaller particles in suspension during that period. Nonetheless, the cumulative sediment flux is small because the observed resuspension is extremely short-lived lasting only a couple of hours in comparison to the turbulent deposition during the intrusion event, which persists for approximately one day. Additionally, there may be deposition of particles due to Stokes settling (and possible more complex mechanisms) during the integration period that, when accounted for, would lower the observed net erosion of sediment. In this case, the reported net erosion is an estimate of the upper bound for the total sediment erosion over the event.

Inflow intrusion speed

The observed maximum and average along-axis velocities within the intrusion bounds during Event II are compared with the estimated velocities from the buoyancy-driven intrusion scaling, $U \approx 0.2Nh$ at both site RO and SP in Fig. 9. As mentioned previously, the vertical extent of the intrusion is indicated by the dark gray lines Fig. 5. Using the temperature measurements interpolated at the upper and lower bounds of the intrusion to obtain $\Delta\rho$ gives an approximation of the average buoyancy frequency across the intrusion, N. The effect of SSC on the density has not been included in this estimate because, in addition to its effect being smaller than that of temperature ($\Delta\rho_{temp} \approx 0.4$ kg m^{-3}), exact values SSC are not known in the intrusion. Nonetheless, the speed of the intrusion based on the scaling is in the range of $U = 0.02$-0.12 m s^{-1} during event II.

At site RO, the intrusion scaling compares well with the observed average along-axis velocity within the intrusion and generally does not exceed the observed maximum velocity (Fig. 9b). At site SP, the buoyancy-driven scaling slightly overestimates the average velocity within the intrusion and more closely follows the observed maximum (Fig. 9c). Most notably, the intrusion-based scaling velocity is significantly larger than the observations late in day 333 at site SP.

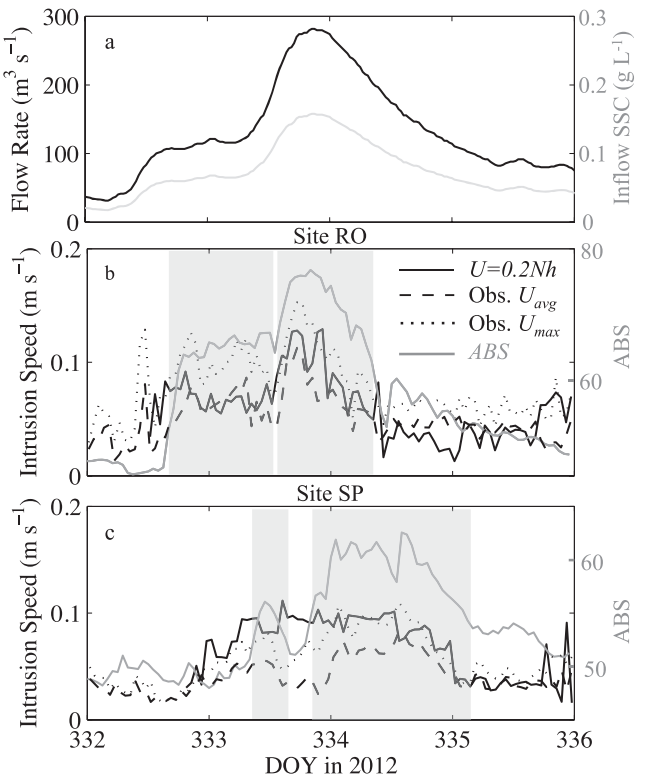

Fig. 9. Time series of Toce River inflow along with the inflow SSC based on a sediment rating curve (a). Time series of velocity (left *y*-axis) from the intrusion scaling ($U = 0.2Nh$), the maximum and average observed along-axis velocity within the intrusion bounds at site RO (b) and site SP (c). The ABS (right *y*-axis) is from the ADCP bin at 46 m depth at site RO (b) and at 47 m depth at SP (c) showing pulses of SSC due to time-varying flow during the event. The gray areas indicate periods of elevated SSC in which the ABS is within 40% of its peak during that period, after subtracting off the minimum ABS over the record.

During this time, the intrusion may be spreading out laterally, and this would lead to an overestimate of the intrusion velocity when using the 2D approximation ($U=0.2Nh$). In general however, the approximate velocity scaling for a 2D buoyancy-driven intrusion appears to compare well with observed velocities during the event, implying that the observed currents are indeed due to buoyancy-driven river intrusions.

Horizontal sediment transport

The rate at which sediment is transported between sites RO and SP can be quantified in a bulk sense using the results of the aforementioned lagged correlation analysis between the SSC averaged over a prescribed range of depths and the observed inflow. The timing of sediment delivery to each of the sites can be determined by examining the time lag corresponding to the peak in the correlation coefficient, *r*. When the SSC is averaged over the entire depth at each site, the peak in the lagged correlation coefficient ($r = 0.79$ and $r = 0.68$ at site RO and SP, respectively) occurred at a lag time of approximately one hour for site RO and a lag time of approximately nine hours for site SP. The difference between the two (eight hours) gives a depth-averaged horizontal transport speed of sediment of 0.05 m s^{-1} between sites RO and SP.

To better quantify the horizontal transport speed of the intrusion, we restrict the depth-averaging to ABS data between 15 m and 50 m (nine and five ADCP bins for site RO and SP, respectively), which corresponds to the approximate time-averaged vertical extent of the intrusion as discussed in relation to the dark gray lines in Fig. 5. The correlation values based on restricting the depth-average to the intrusion were $r = 0.82$ and $r = 0.58$ for sites RO and SP, respectively, where $r > 0.54$ corresponds to $p = 0.01$ with df = 20. The corresponding peaks in the lagged correlation coefficient gave one-hour and six-hour lags for sites RO and SP, respectively. Because site RO is relatively shallow compared to the depth of the intrusion, there is little difference between the lagged correlation results based on the full depth average and the average limited to the depth of the intrusion, both of which are one hour at site RO. However, the depth-averaged time lag over the entire depth at site SP is larger (nine hour) than that which is restricted to the intrusion (six hour). Below the lower extent of the intrusion (50 m depth), sediment experiences weak horizontal transport, and hence the time series of SSC in deeper water is due mostly to sediment settling, thus giving a longer lag time because sediment must be transported both horizontally (short lag) and settle vertically (longer lag) to reach deeper ADCP bins. For reference, the time lag corresponding to layers below the intrusion is approximately 13 h. Therefore, the resulting horizontal sediment transport velocity based on the five-hour lag difference between sites RO and SP based on averaging within the vertical extent of the intrusion is 0.08 m s^{-1}. This time-averaged sediment transport rate over the intrusion depth is comparable to the observed along-axis velocities in the intrusion and to the estimated buoyancy-driven scaling at both sites during Event II, which tend to fluctuate about a mean of 0.08 m s^{-1} (Fig. 9b,c).

The variability of horizontal sediment transport during the large inflow event between sites RO and SP can be investigated by analyzing the SSC time series just below the intrusion depth (approximately 50 m). During Event II, the inflow increases to roughly 100 m^3 s^{-1} during day 332 (left *y*-axis in Fig. 9a), which corresponds to approximately 0.06 g L^{-1} of SSC (right *y*-axis in Fig. 9a) at the river mouth based on a sediment rating curve (Jones 2012) and lasting for approximately one day. This flow rate increase corresponds to a rapid and sustained increase in SSC at site RO as shown by the ABS time series at 47 m depth (right *y*-axis in Fig. 9b). At a later time, there is a small and narrow peak in SSC at site SP indicated by the ABS time series at 46 m depth (right *y*-axis in Fig. 9c). After the one-day period in which the inflow is sustained at 100 m^3 s^{-1}, the flow rate increases to a

peak of 300 $m^3\ s^{-1}$ toward the end of day 333 with an approximate peak in inflow SSC of 0.15 g L^{-1} (Fig. 9a). The increased flow brings in more sediment to the river as indicated by the larger ABS pulses at both sites RO and SP (Fig. 9b,c). The gray shaded areas indicate periods of elevated SSC in which the ABS is within 40% of the peak value within that period after subtracting the minimum ABS value over the record.

The ABS at site RO (Fig. 9b) closely follows the trend in the observed inflow and incoming SSC from the river mouth (Fig. 9a). Additionally, increases in ABS correspond to elevated intrusion velocities and the ABS decays rapidly at the end of the event. In contrast, there is significantly more variability in the observations at site SP, as depicted in Fig. 9c. The ABS signal at site SP during the second pulse (between days 334 and 335) is more spread out in time and the signal decays more slowly at its tail end compared to that at site RO. This is likely due to horizontal dispersion of sediment within the plume, which would generate both a broader pulse and a longer tail.

In contrast to the second peak, the first peak in SSC at site SP (Fig. 9c, day 333.5) is particularly narrow in width compared with the inflow and SSC at site RO. One possible explanation is that the path and the width of the intrusion changes during the event in a way that causes it to bypass the mooring at site SP for a large part of the event. For instance, if the intrusion is confined laterally by the southern boundary of the bay and by rotational forces, then the width of the intrusion, b, is given approximately by $b \sim (QN/f^2)^{1/3} = O(0.1)$km, where Q is approximated by the river inflow rate and N is given by the average buoyancy frequency across the intrusion, as discussed above. Therefore, since site SP is 0.5 km from the southern boundary of the bay, then it is possible that the intrusion is narrow enough during weaker portions of the inflow events that it effectively bypasses site SP, which may explain the narrow first pulse in SSC. The second pulse in Fig. 9c is not as susceptible to this effect owing to a larger flow rate, which reduces the relative effect of Coriolis and leads to a larger plume width, that is, less likely to bypass site SP. It is also possible that while the inflow velocity is smaller, more sediment may settle out of the intrusion before reaching site SP because the sediment effectively has more time to settle before the intrusion is able to reach site SP, although this would not explain the narrowness of the first pulse. Further 3D numerical modeling is needed to investigate the influence of rotation, three-dimensionality, and sediment settling on the inflow intrusion dynamics and we leave this to a future study.

Effective sediment settling throughout the water column

The above analysis and observations imply that between approximately 15 m and 50 m depth, the inflow intrusion and the resulting horizontal transport of SSC dominate the observed sediment dynamics at both sites RO and SP. However, the strength of the intrusion decays owing to dissipation as it flows into the bay and as the river inflow weakens. As a result, sediment, that is, transported horizontally to a particular location by the intrusion eventually begins to settle, particularly as the strength of the turbulence from the intrusion that acts to suspend sediments weakens. Therefore, on settling out of the intrusion, horizontal gradients and vertical turbulent transport become insignificant, and the resulting SSC is described by Eq. 2 in the absence of vertical turbulent transport, viz.

$$\frac{\partial \overline{c}}{\partial t} = w_s \frac{\partial \overline{c}}{\partial z} \tag{5}$$

where w_s is $O(10^{-4}-10^{-6})$m s^{-1} for the silts and clays typically observed in Pallanza Bay. Because sediment delivery based on horizontal transport is so fast relative to that resulting from settling, the two processes are effectively decoupled. That is, a particle trajectory in the bay can be assumed to first follow that due to horizontal transport in the absence of settling, followed by vertical transport due to settling in the absence of horizontal transport.

The decoupling between the horizontal transport and vertical settling of sediment is not apparent at site RO because it is shallow relative to the depth of the intrusion. However, the SSC below the intrusion at site SP (Fig. 10) clearly shows pulses of sediment settling over time. These pulses follow depth-time trajectories (indicated by the representative dashed lines in Fig. 10) that have constant slopes, indicative of constant downward settling rates and negligible horizontal transport. Such behavior was also observed at site SP during the other two inflow intrusion events (15 October and 11 November) that occurred during the deployment (not shown). The depth-time characteristics in Fig. 10 provide qualitative evidence that sediment plumes propagate downward with constant settling rates at site SP. The rate of sediment settling is therefore in the range of 1-7 $\times$ 10^{-3} m s^{-1}

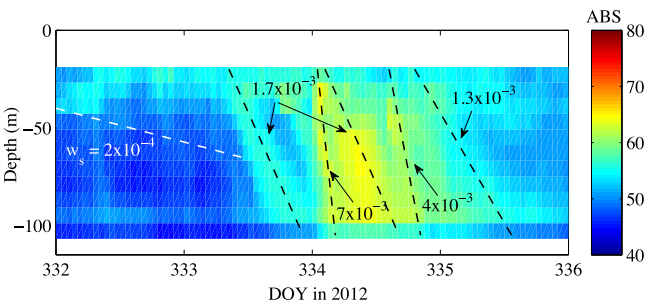

Fig. 10. ABS measured by the ADCP at site SP during Event II with time-space trajectories associated with different sediment settling rates indicated by the dashed lines. The slopes of the trajectories are given by the rate of sediment settling in the range 1.3-7.0 $\times$ 10^{-3} m s^{-1} (black dashed lines) and the expected Stokes setting velocity of $w_s = 2 \times 10^{-4}$ m s^{-1} for a 0.016 mm diameter particle is shown for reference (white dashed line).

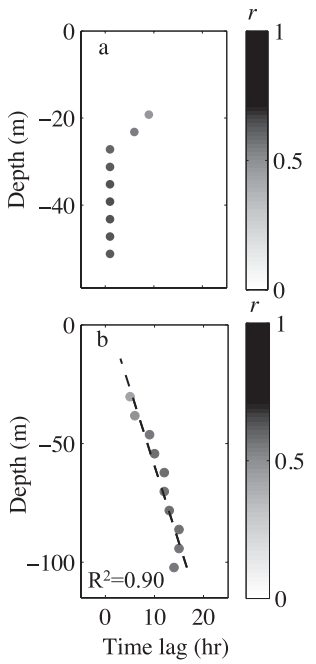

Fig. 11. Depth dependence of the lag time corresponding to the peak in the lagged correlation coefficient, $r(\tau)$, between the river flow rate and the ABS from the ADCP at site RO (a) and site SP (b). Circles indicate data from each ADCP bin where the color denotes the peak value of r, while the dashed line represents the linear fit to the ADCP data. The regression gives a slope of $m = 1.8\times10^{-3}$m s^{-1}.

based on the slopes of the dashed lines in Fig. 10 during Event II, which is consistent with the approximate settling rate from the ABS profiles in Fig. 6 discussed previously. To obtain a Stokes settling velocity of the same magnitude as the observed characteristic slopes, the particle size would need to be approximately 0.062 mm (very fine sand). This is, however, inconsistent with the presence of only silts and clays near site SP with w_s of $O(10^{-4}-10^{-6})$m s^{-1}. The white dashed line in Fig. 10 indicates the larger expected Stokes settling velocity of 2×10^{-4} m s^{-1} (corresponding to a medium silt particle with diameter 0.016 mm), which is one order of magnitude smaller than the observed rates. This discrepancy suggests that other mechanisms are enhancing the rate at which sediment propagates through the water column below the intrusion and we will therefore define w_{eff} as the effective vertical sediment settling velocity observed.

A more quantitative estimate of the effective settling velocity can be obtained by analyzing the depth-dependent lagged correlation between SSC in the water column and the river flow rate. First, the lagged correlation between the SSC time series observed by an ADCP at a given depth below the intrusion, z_s, and the river flow rate time series was computed. Then the time at which the peak correlation occurs was defined as t_s, such that the effective sediment settling can be computed as $w_{\text{eff}} = z_s/t_s$. The depth-dependent time lags (t_s) are shown in Fig. 11a,b for sites RO and SP, respectively. Only values with $r > 0.42$, corresponding to $p = 0.05$ (df = 20), were used in the analysis. The SSC observed above the intrusion was poorly correlated with the inflow and therefore is not shown. At site RO, a time lag of one hour was observed throughout most of the depth indicating that the sediment is delivered at roughly the same time throughout the depth, and the time lag is consistent with the depth-averaged lag results discussed above. The two uppermost data points in Fig. 11a with a longer lag time are above the intrusion depth during some portions of the record, reflecting more complicated dynamics than simple advection that dominates the lower layers. At site SP (Fig. 11b) however, there is a clear linear dependence with depth and the slope of the linear fit to the lag times provides an estimate of the effective settling velocity of sediment averaged throughout the water column and over the entire deployment period. From this analysis, the effective settling rate at site SP is 1.8×10^{-3} m s^{-1}, with $R^2 = 0.90$ for the linear fit. In agreement with the large settling rates evident by the depth-time trajectories in Fig. 10, the time- and depth-averaged settling velocity is also one order of magnitude larger than the expected settling velocity for sediments typically found at site SP.

The large value of the effective settling velocity implies that other mechanisms, in addition to Stokes settling velocity of single particles, appear to be involved in the downward transport of sediment. Based on the linear depth-time trajectories in Fig. 10 and the linear dependence of the lag time with depth in Fig. 11, the effects that increase the effective settling velocity appear to be constant with depth, although different plumes appear to settle at different rates depending on when they arrive in time, as shown in Fig. 10. Although turbulent sediment flux may act to increase the apparent vertical transport of sediment, particularly if its effect were calculated by assuming a steady balance in Eq. 2 ($w_{\text{turb}_{\text{eff}}} = \overline{w'c'}/\overline{c}$), one would expect strong vertical variability in the effective settling velocity calculated in this way given that turbulent effects are small outside of the intrusion or away from boundaries. Furthermore, although turbulence would act to vertically mix or smooth a vertical distribution of sediment over time, one would not expect turbulence to alter the rate at which the mean location of a plume descends through the water column.

Potential mechanisms that may act to increase sediment settling include vertical advection, particle flocculation, and convective or double diffusive type instabilities. Vertical advection could act to produce downward transport at the observed effective settling rate. An estimate of the currents flowing down the slope in Pallanza Bay can be made with the product of the bottom slope (0.01) and the speed of the intrusion (0.10 m s^{-1}) to give a vertical transport speed of 1×10^{-3} m s^{-1}. However, this would only be effective following a particle trajectory down the slope and not necessarily following a particle as it moves downward at a fixed

horizontal location, as indicated by the trajectories in Fig. 10. Time-variable river flow rates would also produce time-variable vertical transport rates. A more likely cause of the increased vertical settling rate is particle aggregation or flocculation of fine sediments. Although this effect is typically neglected in freshwater systems due to the absence of the electrostatic effects of salinity, flocculation has more recently been shown to alter the particle settling velocity in freshwater systems (Droppo et al. 1997; Guo and He 2011). In the absence of salinity, flocculation is a function of organic content, biochemical properties, concentration, and turbulence. Flocculation can enhance the particle settling velocity by orders of magnitude depending on floc size and effective density. Guo and He found that the settling velocity in freshwater portions of the Yangtze River varied between 0.7 and 2×10^{-3} m s^{-1}, which is within the range of the settling velocities we observe in Pallanza Bay and is one order of magnitude larger than the expected Stokes settling velocity. Additionally, in the case of large SSC in the intrusion, convective or double-diffusive instabilities can generate rapid settling of particles in the water column (Maxworthy 1999; Parsons et al. 2001; Burns and Meiburg 2012). The effect of sediment density and decaying turbulence within the intrusion can potentially generate fingering or leaking of sediment downward at rates up to 20 times the Stokes settling velocity (Burns and Meiburg 2012), which is consistent with the order of magnitude discrepancy observed in Pallanza Bay. Despite the likelihood of these complex processes impacting the observed settling, no in situ grain size measurements or sediment samples were taken nor were turbulence measurements made within the intrusion, and thus the effect of the processes could not be verified.

Sediment dynamics in Pallanza Bay

The objective of this study was to determine the dominant mechanisms controlling suspended sediment transport in a large alpine lake. Observations over a three-month period show that river inflow intrusions and deposition dominate the suspended sediment dynamics in the system and only small amounts of sediment resuspension were observed. The study provides unique observations of sediment delivery both horizontally between a site near the river outflow and a site deeper in the bay and vertically from the inflow intrusion to the sediment bed. The rate of sediment delivery between the two sites is consistent with velocity scaling for a 2D inflow intrusion driven by the density difference between the cold river waters and the warmer lake. The near-bed turbulent sediment flux term was shown to significantly impact the rates of deposition during inflow intrusions. Furthermore, the rate of sediment settling through the water column from an inflow intrusion was shown to be one order of magnitude larger than the expected Stokes settling velocity. Therefore, other mechanisms such as particle flocculation or convective instabilities may drive elevated settling velocities although these effects could not be quantified. The river inflow is the most significant mechanism governing sediment transport in a large alpine lake and the dynamics of the inflow and the intrusion in the lake are likely to vary seasonally with changing stratification.

References

Alavian, V., G. H. Jirka, R. A. Denton, M. C. Johnson, and H. G. Stefan. 1992. Density currents entering lakes and reservoirs. J. Hydraulic Eng. **118**: 1464-1489. doi:10.1061/(ASCE)0733-9429(1992)118:11(1464)

Bedford, K., O. Wai, C. Libicki, and R. Van Evra, III. 1987. Sediment entrainment and deposition measurements in Long Island Sound. J. Hydraulic Eng. **113**: 1325-1342. doi:10.1061/(ASCE)0733-9429(1987)113:10(1325)

Best, J., R. A. Kostaschuk, J. Peakall, P. V. Villard, and M. Franklin. 2005. Whole flow field dynamics and velocity pulsing within natural sediment-laden underflows. Geology **33**: 765-768. doi:10.1130/G21516.1

Brand, A., J. R. Lacy, K. Hsu, D. Hoover, S. Gladding, and M. T. Stacey. 2010. Wind-enhanced resuspension in the shallow waters of South San Francisco Bay: Mechanisms and potential implications for cohesive sediment transport. J. Geophys. Res. **115**: C11024. doi:10.1029/2010JC006172

Brennan, M. L., D. H. Schoellhamer, J. R. Burau, and S. G. Monismith. 2002. Tidal asymmetry and variability of bed shear stress and sediment bed flux at a site in San Francisco Bay, USA. Proc. Mar. Sci. **5**: 93-107. doi:10.1016/S1568-2692(02)80010-9

Burns, P., and E. Meiburg. 2012. Sediment-laden fresh water above salt water: Linear stability analysis. J. Fluid Mech. **691**: 279-314. doi:10.1017/jfm.2011.474

Callieri, C. 1997. Sedimentation and aggregate dynamics in Lake Maggiore, a large, deep lake in Northern Italy. Mem. Ist. Italiano di Idrobiol. **56**: 37-50.

Chikita, K. 1990. Sedimentation by river-induced currents: Field measurements and interpretation. Sedimentology **37**: 891-905. doi:10.1111/j.1365-3091.1990.tb01832.x

Chua, V. P., and O. B. Fringer. 2011. Sensitivity analysis of three-dimensional salinity simulations in North San Francisco Bay using the unstructured-grid SUNTANS model. Ocean Modell. **39**: 332-350. doi:10.1016/j.ocemod.2011.05.007

Chung, S. W., M. R. Hipsey, and J. Imberger. 2009. Modelling the propagation of turbid density inflows into a stratified lake: Daecheong Reservoir, Korea. Environ. Modell. Softw. **24**: 1467-1482. doi:10.1016/j.envsoft.2009.05.016

DeCesare, G., J.-L. Boillat, and A. J. Schleiss. 2006. Circulation in stratified lakes due to flood-induced turbidity currents. J. Environ. Eng. **132**: 1508-1517. doi:10.1061/(ASCE)0733-9372(2006)132:11(1508)

Deines, K. L. 1999. Backscatter estimation using Broadband acoustic Doppler current profilers, p. 249-253. In S. P.

Anderson, E. A. Terry, J. A. R. White and A. J. William [eds.], Proceedings of the IEEE Sixth Working Conference on Current Measurement Technology. doi:10.1109/CCM.1999.755249

Droppo, I. G., G. G. Leppard, D. T. Flannigan, and S. N. Liss. 1997. The freshwater floc: A functional relationship of water and organic and inorganic floc constituents affecting suspended sediment properties. Water Air Soil Pollut. **99**: 43-54. doi:10.1007/BF02406843

Ford, D. E., and M. C. Johnson. 1983. An assessment of reservoir mixing processes. Technical Report E-83-7. Ford, Thornton, Norton and Associates, Ltd. (for the U.S. Army Engineer Waterways Experiment Station). Vicksburg, MS.

Fringer, O. B., M. Gerritsen, and R. L. Street. 2006. An unstructured-grid, finite-volume, nonhydrostatic, parallel coastal-ocean simulator. Ocean Modell. **14**: 139-278. doi:10.1016/j.ocemod.2006.03.006

Fugate, D. C., and C. T. Friedrichs. 2002. Determining concentration and fall velocity of estuarine populations using ADV, OBS and LISST. Cont. Shelf Res. **22**: 1867-1886. doi:10.1016/S0278-4343(02)00043-2

Gartner, J. W. 2004. Estimating suspended solids concentrations from backscatter intensity measured by acoustic Doppler current profiler in San Francisco Bay, California. Mar. Geol. **211**: 169-187. doi:10.1016/j.margeo.2004.07.001

Gloor, M., A. Wüest, and M. Münnich. 1994. Benthic boundary mixing and resuspension induced by internal seiches. Hydrobiologia **284**: 59-68. doi:10.1007/BF00005731

Guo, L., and Q. He. 2011. Freshwater flocculation of suspended sediments in the Yangtze River, China. Ocean Dyn. **61**: 371-386. doi:10.1007/s10236-011-0391-x

Ha, H. K., W.-Y. Hsu, J. P.-Y. Maa, Y. Y. Shao, and C. W. Holland. 2009. Using ADV backscatter strength for measuring suspended cohesive sediment concentration. Cont. Shelf Res. **29**: 1310-1316. doi:10.1016/j.csr.2009.03.001

Imberger, J., and P. F. Hamblin. 1982. Dynamics of lakes, reservoirs, and cooling ponds. Ann. Rev. Fluid Mech. **14**: 153-187. doi:10.1146/annurev.fl.14.010182.001101

Jones, C. 2012. Idrodinamica e trasporto dei sedimenti nella Baia di Pallanza. Technical Report. Sea Engineering (for ENVIRON Italy). Santa Cruz, CA.

Kawanisi, K., and S. Yokosi. 1997. Characteristics of suspended sediment and turbulence in a tidal boundary layer. Cont. Shelf Res. **17**: 859-875. doi:10.1016/S0278-4343(96)00066-0

Lorke, A. 2007. Boundary mixing in the thermocline of a large lake. J. Geophys. Res. **112**: C09019. doi:10.1029/2006JC004008

Maa, J. P.-Y., and J.-I. Kwon. 2007. Using ADV for cohesive sediment settling velocity measurements. Estuar. Coast. Shelf Sci. **73**: 351-354. doi:10.1016/j.ecss.2007.01.008

Manins, P. C. 1976. Intrusion into a stratified fluid. J. Fluid Mech. **74**: 547-560. doi:10.1017/S0022112076001948

Marchetto, A., A. Lami, S. Musazzi, J. Massaferro, L. Langone, and P. Giulizzoni. 2004. Lake Maggiore (N. Italy) trophic history: Fossil diatom, plant pigments and chironomids, and comparison with long-term limnological data. Quat. Int. **113**: 97-110. doi:10.1016/S1040-6182(03)00082-X

Mariani, G., and others. 2008. Atmospheric input of POPs into Lake Maggiore (Northern Italy): PBDE concentrations and profile in the air, precipitation, settling material and sediments. Chemosphere **73**: S114-S121. doi:10.1016/j.chemosphere.2007.02.071

Maxworthy, T. 1999. The dynamics of sedimenting surface gravity currents. J. Fluid Mech. **392**: 27-44. doi:10.1017/S002211209900556X

Mellor, G. L., and T. Yamada. 1982. Development of a turbulence closure model for geophysical fluid problems. Rev. Geophys. **20**: 851-875. doi:10.1029/RG020i004p00851

Morris, G. L., G. Annandale, and R. Hotchkiss. 2008. Reservoir sedimentation, p. 579-612. In M. Garcia [eds.], Sedimentation engineering. American Society of Civil Engineers.

Münnich, M., A. Wüest, and D. M. Imboden. 1992. Observations of the second vertical mode of the internal seiche in an alpine lake. Limnol. Oceanogr. **37**: 1705-1719. doi:10.4319/lo.1992.37.8.1705

Parsons, J. D., J. W. Bush, and J. P. M. Syvitski. 2001. Hyperpycnal plume formations from riverine outflows with small sediment concentrations. Sedimentology **48**: 465-478. doi:10.1046/j.1365-3091.2001.00384.x

Rueda, F. J., and S. MacIntyre. 2010. Modelling the fate and transport of negatively buoyant storm-river water in small multi-basin lakes. Environ. Modell. Softw. **25**: 146-157. doi:10.1016/j.envsoft.2009.07.002

Salehi, M., and K. Strom. 2011. Using velocimeter signal to noise ratio as a surrogate measure of suspended mud concentration. Cont. Shelf Res. **31**: 1020-1032. doi:10.1016/j.csr.2011.03.008

Schallenberg, M., and C. W. Burns. 2004. Effects of sediment resuspension on phytoplankton production: Teasing apart the influences of light, nutrients and algal entrainment. Freshw. Biol. **49**: 143-159. doi:10.1046/j.1365-2426.2003.01172.x

Schoellhamer, D. H., T. E. Mumley, and J. E. Leatherbarrow. 2007. Suspended sediment and sediment-associated contaminants in San Francisco Bay. Environ. Res. **105**: 119-131. doi:10.1016/j.envres.2007.02.002

Shimizu, K., J. Imberger, and M. Kumagai. 2007. Horizontal structure and excitation of primary motions in a strongly stratified lake. Limnol. Oceanogr. **56**: 2641-2655. doi:10.4319/lo.2007.52.6.2641

Thorne, P. D., and D. M. Hanes. 2002. A review of acoustic measurement of small-scale sediment processes. Cont. Shelf Res. **22**: 603-632. doi:10.1016/S0278-4343(01)00101-7

Trowbridge, J. H., W. R. Geyer, M. M. Bowen, and A. J. Williams. 1999. Near-bottom measurements in a partially

mixed estuary: Turbulent energy balance, velocity structure, and along-channel momentum balance. J. Phys. Oceanogr. **29**: 3056-3072. doi:10.1175/1520-0485(1999)029<3056:NBTMIA>2.0.CO;2

Umeda, M., K. Yokoyama, and T. Ishikawa. 2006. Observation and simulation of floodwater intrusion and sedimentation in the Shichikashuku Reservoir. J. Hydraulic Eng. **132**: 881-891. doi:10.1061/(ASCE)0733-9429(2006)132:9(881)

Van Prooijen, B. C., and J. C. Winterwerp. 2010. A stochastic formulation for erosion of cohesive sediments. J. Geophys. Res. **115**: C01005. doi:10.1029/2008JC005189

van Rijn, L. C. 1984. Sediment transport, part II: Suspended load transport. J. Hydraulic Eng. **110**: 1613-1641. doi: 10.1061/(ASCE)0733-9429(1984)110:11(1613)

Vidal, J., R. Marcé, T. Serra, J. Colomer, F. Rueda, and X. Casamitjana. 2012. Localized algal blooms induced by river inflows in a canyon type reservoir. Aquat. Sci. **74**: 315-327. doi:10.1007/s00027-011-0223-6

Voulgaris, G., and S. T. Meyers. 2004. Temporal variability of hydrodynamics, sediment concentration and sediment settling velocity in a tidal creek. Cont. Shelf Res. **24**: 1659-1683. doi:10.1016/j.csr.2004.05.006

Winterwerp, J. C., and W. G. M. van Kesteren. 2004. Introduction to the physics of cohesive sediment in the marine environment. Elsevier.

Yuan, Y., H. Wei, L. Zhao, and W. Jiang. 2008. Observations of sediment resuspension and settling off the mouth of Jiaozhou Bay, Yellow Sea. Cont. Shelf Res. **28**: 2630-2643. doi:10.1016/j.csr.2008.08.005

Acknowledgments

We would like to thank Diana Lin and Richard Luthy for providing data from simultaneous measurements of sediment properties and deposition and Alessandro Oggioni and Craig Jones for sharing bathymetry datasets. Craig Jones and Sea Engineering also provided helpful insight into understanding the sediment dynamics at our site. We are grateful to Ryan Walter and Ryan Moniz for providing help with mooring design and with mooring deployment and recovery. Finally, we thank Elaine Hart and two anonymous reviewers who contributed to improvement in the quality and clarity of the manuscript. This work was made possible through a grant from Eni S.p.a. under research agreement number 2500004072. We are grateful for the support of Eni scientific officers Giuliana Franzosi, Raffaello Sisto, Pietro Cesti, and Luciano Zaninetta, and for the logistical support for the field campaign provided by Eni, Syndial, Environ, Carma Coring, Sub Verbania, and Cantiere del Verbano in Italy. The fieldwork would not have been possible without the help and support of Giorgio Bianchi, Elisa Bizzotto, Martina Cecchetto, Stefano Fioletti, Federico Santoro, Massimo Magagnoli, Renato Brughera, and Aldo Bottagisio.

Received 12 September 2014
Amended 20 January 2015
Accepted 4 March 2015

Associate editor: Dr. John Downing